Holographic optical trapping of microrods and nanowires

Stephen H. Simpson and Simon Hanna*

H.H. Wills Physics Laboratory, University of Bristol, Tyndall Avenue, Bristol BS8 1TL, UK
*Corresponding author: S.Hanna@bristol.ac.uk

Holographic optical tweezing permits the trapping of objects with less than spherical symmetry in appropriately distributed sets of beams thereby permitting control to be exerted over both the orientation and position. In contrast to the familiar case of the singly trapped sphere, the stiffness and strength of such compound traps will have rotational components. We investigate this for a simple model system consisting of multiply trapped dielectric cylinder. Optically induced forces and torques are evaluated using the discrete dipole approximation and the resulting trap stiffnesses are presented. A variety of configurations of trapping beams are considered. Hydrodynamic resistances for the cylinder are also calculated and used to estimate translation and rotation rates. A number of conclusions are reached concerning the optimal trapping and dragging conditions for the rod. In particular, it is clear that it is advantageous to drag a rod in a direction perpendicular rather than parallel to its length. In addition, it is observed that the polarization of the incident light plays a significant role. Finally, it is noted that the non-conservative nature of the optical force field manifests itself directly in the stiffness of the trapped cylinder. The consequences of this last point are discussed. © 2010 Optical Society of America

OCIS codes: 350.4855, 050.1755, 140.7010, 290.5850.

1. INTRODUCTION

In this paper, we consider the forces and torques that may be applied to microrods, nanowires, or other cylindrical structures, when held in multiple optical traps. The most common system encountered in optical trapping experiments is that of the dielectric microsphere held in a tightly focused linearly polarized Gaussian beam. The optically induced forces that are experienced arise from electromagnetic stresses distributed over the sphere's surface. These stresses are proportional to the light intensity and are directed normally to the surface [1,2]. Evaluating the gradient of the force at the equilibrium position gives a tensor, known as the trap *stiffness*. Symmetry dictates that the stiffness tensor must be symmetric in this case, with three distinct eigenvalues, since it is diagonalized by aligning the coordinate axes with the beam axis, polarization direction, and their mutual normal [3,4].

A second characteristic quantity of the trap is its strength, as expressed by the maximum restoring force that it can exert. This parameter is direction dependent, but it is usually considered sufficient to quote its value in specific directions. Because of its fundamental significance, the trapped sphere has been subjected to a great deal of experimental and theoretical analysis [5–7].

However, when the complexity of the system is increased even slightly, the same cannot be said. There are, to the best of our knowledge, no calculations or measurements of the full stiffness matrix of any optically trapped non-spherical object in the literature, whether singly or multiply trapped. Given that holographic optical trapping is now a mature widely used technology, and that the trapping and manipulation of low symmetry objects in multiple beams is increasingly common, this seems surprising. However, as discussed below, such investigations can be problematic, both computationally and experimentally.

Nevertheless, in this paper we embark on a comprehensive study of the characteristic parameters of multiply trapped dielectric microrods. Such rods have been used in a number of practical applications. For example, they have been used as scanning optical probes in a novel form of near-field microscope [8], as force transducers in novel force microscopes [9], in the fabrication of nanoelectronic devices [10], as components in larger structures [11,12], and as a model for swimming bacteria [13].

For the purposes of the current study, we calculate the optically induced force as a function of the position and orientation of a dielectric cylinder with respect to a variety of different beam configurations. Trap strengths are noted and trap stiffnesses are evaluated. The hydrodynamic resistance of the cylinder is also calculated and used to estimate the maximum drag and rotation rates that the traps are capable of delivering. A number of conclusions are reached concerning the nature of the stiffness matrix and optimal conditions for trapping and dragging cylinders. In particular, it is noted that the stiffness matrix takes a variety of forms depending on the symmetry of the arrangement of trapping beams; by virtue of the non-conservative nature of optically induced forces it will be, in general, non-symmetric. In the following sections we provide some background theory and the details of our calculation methods, before presenting the results of cal-

culations of the forces and torques imposed on a dielectric cylinder by a variety of different arrangements of Gaussian beams.

2. BACKGROUND THEORY

For a particle formed from a non-absorbing optically isotropic material the body forces arise from combinations of electromagnetic stresses distributed over its surface. The cycle-averaged force and torque densities, $\langle \mathbf{f} \rangle$ and $\langle \mathbf{t} \rangle$, respectively, are given by [2]

$$\langle \mathbf{f} \rangle = \tfrac{1}{4}|\mathbf{E}|^2 \Delta \epsilon \delta(\mathbf{n})\hat{\mathbf{n}}, \tag{1a}$$

$$\langle \mathbf{t} \rangle = \mathbf{r} \times \langle \mathbf{f} \rangle, \tag{1b}$$

where $\mathbf{E}$ is the total electric field, $\Delta \epsilon$ is the dielectric contrast, and $\delta(\mathbf{n})$ indicates a Dirac delta function concentrated on the material boundary with $\mathbf{n}$ being the surface normal. $\mathbf{r}$ is a position vector. The total body forces are derived from these densities by integration over all space which, by virtue of the delta function, reduces to integration over the surface of the particle. The forces result, therefore, from imbalances in the light intensity over the surface of the particle. These imbalances are introduced either by the incident field or through optical scattering.

The forces and torques that can act in any trapping scenario are subject to symmetry conditions. If the force density contains a mirror plane, the component of the force perpendicular to that mirror must be zero, as must be the torque about any axis in that plane. If there is an axis of cylindrical symmetry, the components of force and torque perpendicular to this axis must also be zero.

Optical torques are subject to a further restriction based only on the geometry of the particle. For a body with cylindrical symmetry, the position vector of any point on its surface and the vector normal to its surface either must be parallel, in which case the torque density is zero, or must span a plane that includes the symmetry axis, in which case the torque density must be normal to the symmetry axis. Consequently, a body with cylindrical symmetry cannot feel an optically induced torque about its symmetry axis.

In this paper we are concerned with locating equilibrium configurations of a multiply trapped dielectric rod, and with evaluating forces and torques around this position. Generalized stiffness matrices are calculated by taking the gradient of the generalized force (i.e., force + torque), at the equilibrium position. This last quantity is a matrix of order 6, consisting of a 2×2 array of tensors [4], that provides a linear approximation to the generalized force as a function of the displacement,

$$\mathbf{K} = \begin{pmatrix} \mathbf{K}^{tt} & \mathbf{K}^{tr} \\ \mathbf{K}^{rt} & \mathbf{K}^{rr} \end{pmatrix}. \tag{2}$$

The two sub-tensors, $\mathbf{K}^{tt}$ and $\mathbf{K}^{rr}$, are formed by taking the derivatives of the forces with respect to the translational displacements, and the torques with respect to the rotational coordinates. $\mathbf{K}^{tt}$ therefore gives restoring forces as a function of the translation, while $\mathbf{K}^{rr}$ gives restoring torques as a function of the angular displacement. The coupling pseudo-tensors, $\mathbf{K}^{tr}$ and $\mathbf{K}^{rt}$, contain derivatives

of the force with respect to the angular displacement, and of the torque with respect to the translational displacement. See [4] for a more complete discussion. As will be seen, the behavior of each of the elements of $\mathbf{K}$ is compatible with, and explainable in terms of, the principles discussed above.

In the low Reynolds number regime, the applied force is linearly related to the velocity via the hydrodynamic resistance matrix. This quantity is also calculated for the cylinder in question.

3. COMPUTATIONAL METHODS

A. Optical Calculations
The required optical calculations may be performed in several different ways but, in general, they fall into two discrete parts. First of all a solution is sought to the optical scattering problem. Next, the knowledge of the total fields is used to evaluate the associated rates of change of the electromagnetic momentum. By Newton's third law, these latter quantities give the forces on the particle.

The optical scattering problem can be dealt with by a range of techniques. Numerical techniques, such as the finite difference time domain (FDTD) method [14,15] or the finite element method [16], provide enormous flexibility at the cost of computational overheads. Semi-analytical methods, such as the T-matrix method [17–20] or the multiple multipole method [21], are more restrictive in their application or require special adaptations to be made for each new situation. The T-matrix method, in particular, suffers from convergence problems that render it unsuitable for the treatment of objects of high aspect ratios [22,23].

The force calculation typically involves an integration of the electromagnetic momentum flux over a closed surface surrounding the trapped object. The precise manner in which this is achieved depends on the method used to acquire the fields. In the FDTD method it amounts to a direct numerical integration of linear functions of the Maxwell's stress tensor, while in the T-matrix method the same integration can be performed analytically.

For the present work, we have selected the discrete dipole approximation (DDA). Although less flexible than the FDTD method, especially regarding complicated sets of boundary conditions, it has the advantage that the fields surrounding the scatterer need not be modeled. In addition the large dense set of linear equations associated with the DDA are amenable to sophisticated iteration schemes that permit a rapid solution for relatively large systems. In the following subsection salient details of our implementation of this method are given.

B. Discrete Dipole Approximation
The DDA has been used widely in scattering problems [24,25] and has recently been applied in the field of optical trapping [26–28]. Several public domain DDA codes exist [29], suited for tackling general problems in light scattering. However, for the purposes of performing simulations of optical trapping it is preferable to use a code tailored for this specific application. It is advantageous, for example, to be able to introduce arbitrarily positioned sets of beams of the kinds encountered in holographic op-

tical trapping, to be able to reposition beams and particles either as desired or in accordance with the integrated equations of motion of the simulated particles, or to be able to conduct numerical searches for equilibrium configurations. In the following paragraphs we provide an outline of the DDA method and document the characteristics peculiar to our implementation.

In the DDA method, the scattering object is represented by an array of dipolar point polarizabilities. These dipoles are located on the nodes of a square lattice that fall within the surface of the object. By assigning their polarizabilities appropriately, the optical properties of the discretized model object tend toward those of the real object, as the lattice is refined. We use the polarizability devised by Draine [30], in which finite phase changes are accounted for via the inclusion of a small imaginary term,

$$\alpha = \frac{\alpha_{CM}}{1 - i\frac{2}{3}k^3\alpha_{CM}}, \tag{3}$$

where α_{CM} is the Clausius–Mossotti polarizability; $\alpha_{CM} = a^3(\epsilon_s - \epsilon_m)/(\epsilon_s + 2\epsilon_m)$, with a being the radius of a sphere whose volume is equivalent to that of one cell of the cubic lattice; and ϵ_s and ϵ_m are the relative permittivities of the object and the background medium, respectively. This corrective term takes account of the finite wavelength, ensures compatibility with the optical theorem [30], and is necessary for the correct rendering of the contribution to the force deriving from radiation pressure [31]. The point polarizabilities are coupled via the dipole interaction tensor so that the local field to which each polarizability is exposed is given by the sum of the incident field and the dipole fields radiated by all other polarizabilities. In addition, the polarization at each lattice site is given by the product of the local field and the polarizability,

$$\mathbf{E}_j = \mathbf{E}_j^{inc} - \sum_{k=1,..,N;\ k \neq j} \mathbf{A}_{jk}\mathbf{P}_k, \tag{4}$$

$$\mathbf{P}_k = \alpha\mathbf{E}_k. \tag{5}$$

Here, the subscripts label the lattice sites, $\mathbf{E}_j$ is the total electric field, $\mathbf{E}_j^{inc}$ is the incident electric field, and $\mathbf{P}_j$ is the polarization. $\mathbf{A}_{jk}$ is the dipole interaction tensor that, when multiplied by $\mathbf{P}_k$, gives the electric field at site j due to the polarization of site k. There are N lattice sites lying within the scatterer. These equations can be written more compactly as

$$\mathbf{E}_j^{inc} = \sum_{k=1,..,N} \overline{\mathbf{A}}_{jk}\mathbf{P}_k, \tag{6}$$

$$\overline{\mathbf{A}}_{jk} = \begin{cases} \mathbf{A}_{jk}, & j \neq k \\ 1/\alpha, & j = k, \end{cases} \tag{7}$$

where $\overline{\mathbf{A}}$ is the *interaction matrix*. This is a dense set of $3N$ linear equations, in $3N$ unknowns, whose solution consists of finding the polarization of each lattice site. These polarizations may then be used to determine the radiation forces and torques.

The solution to the discretized problem, and therefore the values of all derived quantities, tends toward that of the real continuous system as the lattice is refined. The degree of refinement required depends on the optical size of the object being modeled; a commonly used rule is that the lattice parameter should be less than one tenth of a wavelength in the medium from which the scattering object is composed [24]. The lattice must also be fine enough to resolve all significant geometrical features.

The number of lattice sites used in a typical calculation, N, might number $\sim 10^6$ or more. As a consequence it is customary to solve the system iteratively using a Krylov method [32]. Many such algorithms have been applied to the DDA equations [25]. For the current purposes we find that the quasi-minimal residual method and the biconjugate gradient method are adequate and, in some ways, preferable [33]. Their relative simplicity is advantageous from the point of view of both the memory requirements and the operation count per iteration. In addition, we find that they converge rapidly and reliably in all of the instances treated below.

Each iteration of a Krylov method [32] consists of a sequence of simple matrix and vector operations performed in a $3N$ dimensional vector space. The most expensive of these, computationally, are matrix-vector products, which require $O(N^2)$ basic operations. The linear algebra can be expedited by exploiting the fact that the dipole interaction matrix $\mathbf{A}_{jk}$, as it appears in Eq. (4), is a function only of the lattice vector; $\mathbf{A}_{jk}$ does not depend explicitly on the site coordinates, r_j or r_k, only on their difference. This reduces the required storage and, more importantly, it means that matrix-vector products take the form of convolutions which can be evaluated using fast Fourier transforms (FFTs), thereby reducing the operation count to $O(N \ln(N))$.

Finally, the radiation force and torque are evaluated using formulas based on the negative gradient of the classical dipole interaction Hamiltonian [34,35]. These calculations also involve matrix-vector products which can again be accelerated by the FFT [36]. In our implementation, the FFTs are computed using the public domain software, FFTW [37]. This software is multithreaded, as is the rest of the DDA code in which it is embedded.

C. Gaussian Beam Specification
For each simulation, an appropriately defined set of incident fields is required. For the current purpose, this amounts to sets of linearly polarized Gaussian beams. It is necessary to evaluate the incident field on each lattice point within the object, i.e., $O(10^6)$ evaluations. Therefore, it is useful to have a closed form expression of the field components that can be evaluated quickly and reliably. For this, we use complex source point (CSP) beams [38,39] (see the Appendix). The force calculation requires total field derivatives as well as the fields themselves. While the gradients of the local field, due to the scattering of the surrounding polarizabilities, can be calculated from the gradient of the dipole interaction tensor [34], the gradient of the incident field can be calculated directly from the relatively simple equations defining the beam [see Eqs. (A1)–(A3)].

Rigid transformations of the beam equation, and its derivatives, are required to establish the desired configuration of beams, to effect the relative motion between the particle and the beams, and to perform force calculations

in the appropriate fields. For a transformation consisting of a translation through a vector r_0, and a rotation represented by a matrix R, a vector field transforms as

$$\psi(r) \to R \cdot \psi(R^{-1} \cdot r) + r_0, \tag{8}$$

while the gradient of the vector field transforms as

$$\nabla \psi(r) \to R \cdot \nabla \psi(R^{-1} \cdot r) \cdot R^{-1} + r_0. \tag{9}$$

Calculated forces and torques need to be normalized against the optical power in the incident field. Since beams in close proximity will interfere, we calculate the incident field power by numerically integrating the Poynting vector over a plane perpendicular to the axes of the beams.

D. Mechanical Equilibrium
As mentioned above we are interested not only in the forces and torques, but also in the locations of mechanical equilibria and the gradient of the force evaluated at these points. In the most symmetric configuration considered below, the conditions under which all of the forces vanish, except for that parallel to the beam (z-axis), are dictated by mirror symmetry. The z-coordinate of the equilibrium position can then be found by a binary search. When the beam symmetry is lower, more coordinates need to be included in the search and we use the conjugate gradient method [40]. Subsequently, gradients are found, numerically, by evaluating the forces at five points centered at equilibrium. The separation of these points, Δ, is 10 nm for translations and 4×10^{-3} rad for rotations. The derivative with respect to a general coordinate x is then calculated from the third order accurate formula [41],

$$f'(x) \approx \frac{-f(x+2\Delta) + 8f(x+\Delta) - 8f(x-\Delta) + f(x-2\Delta)}{12\Delta}. \tag{10}$$

E. Hydrodynamic Calculations
The hydrodynamic resistance of the cylinder is also required. We evaluate the friction coefficients for the cylinder, numerically, using bead models [42,43]. In a manner analogous to the DDA method, the body of interest is represented by an array of beads that are coupled, this time, by the Rotne–Prager interaction tensor. We use the "rough shell" variant [43], in which the beads representing the object are located on a square lattice, but the interior beads are removed, since they do not influence the result of the calculation. The large, dense, and linear set of equations that result from the coupling interactions must be solved directly. We achieve this step using the public domain package, ScaLAPACK [44], distributing the matrix inversion over eight processors. This allows us to consider models consisting of large numbers of beads, typically $\sim 10^4$.

4. RESULTS

In this section we first examine the convergence properties of force calculations based on the DDA method by varying the lattice parameter δ. We then present the re-

sults of calculations of the forces and torques imposed on a dielectric cylinder by a variety of parallel arrangements of Gaussian beams.

The rod considered is 5 μm in length, has a radius of 0.2 μm, and resides in an aqueous solvent with a refractive index of $n_w = 1.333$. It has a relative refractive index of $n_{cylinder}/n_w = 1.1$, corresponding to a silica glass. The arrangement of the beams varies between calculations, but in each case the frequency of the radiation is 3.75×10^{14} Hz. The CSP beam is further specified by setting $z_0 = 3/k_w$ (see the Appendix), where k_w is the wavenumber in water, giving a beam waist radius of half the wavelength in water, $\lambda_w/2$.

The simulation geometry is shown in Fig. 1. The cylinder is initially positioned, symmetrically, so that it intersects with the foci of a set of parallel traps. The cylinder axis is taken parallel to x, and the +ve z-axis is taken down the beam. The origin of the coordinate frame is coincident with the center of the cylinder in this initial position. The rotation angles, θ_x, θ_y, and θ_z, are taken as rotations about the coordinate axes, where the origin for rotations is coincident with the center of the cylinder. The torques quoted are referred to the same center; for example, τ_z refers to the torque about the z-axis, through the center of the rod.

The resistance matrix for a cylindrically symmetric object is diagonal [45]. Using the bead model described above, we find the translational friction coefficients to be 1.3×10^{-2} pN s/μm in the direction parallel to the cylinder axis and 1.9×10^{-2} pN s/μm in the transverse directions. Rotations about axes perpendicular to the cylinder axis experience a friction of 6.3×10^{-2} pN μm s/rad, while about the cylinder axis the resistance is 2.5×10^{-3} pN μm s/rad.

A. Convergence
Figure 2 shows force and torque calculations for a silica cylinder trapped horizontally in two parallel beams (4.4 μm separation), subject to a small arbitrary displacement as the lattice parameter for the DDA calculation, δ, is varied. It can be seen that the results of the calculations vary in an irregular manner until δ reaches about 0.02 μm, or $\sim\lambda/30$, where λ is the wavelength in the particle. This degree of refinement is in excess of the $\lambda/10$ rule for spheres quoted above [24]. This more stringent demand may result from the anisotropy of the trapped
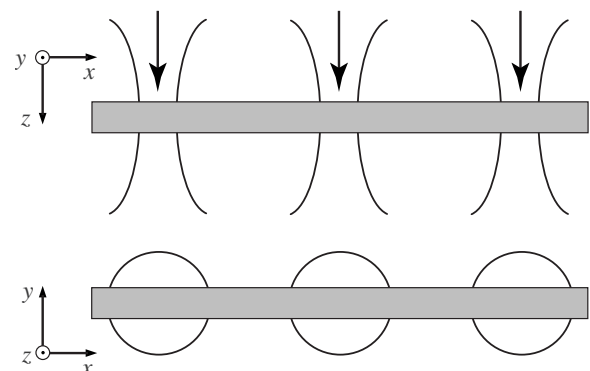

Fig. 1. Schematic showing a typical initial simulation geometry with a cylinder held in a parallel linear array of Gaussian beams.
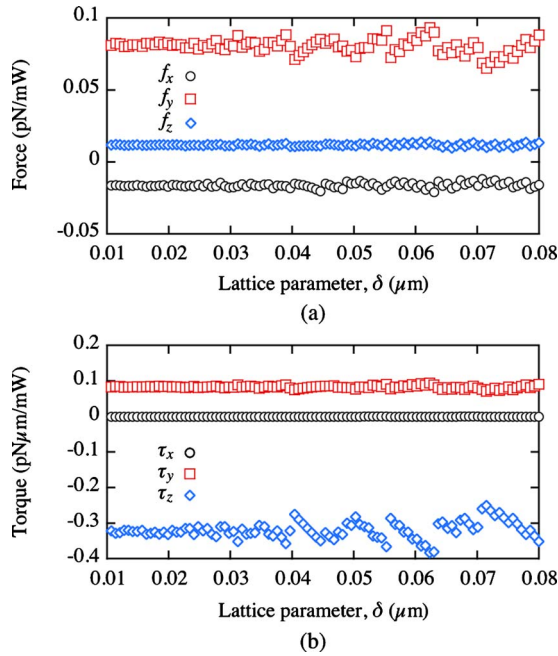
Fig. 2. (Color online) Calculations of (a) the forces and (b) the torques acting on a displaced cylinder with a radius of 0.2 μm and a length of 5 μm, held in two parallel traps, as functions of the DDA lattice parameter δ. In (a) the cylinder is displaced by 0.1 μm along the x- and y-axes, while in (b) it is rotated by 0.1 rad about each axis.

particle. It could, also, be connected with the nature of our force calculations compared with the calculations in [24].

As expected, the induced torque about the cylinder axis, τ_x, vanishes due to rotational symmetry. Numerically, this condition is not satisfied identically. However, the error is very small: calculated values of τ_x are $\approx 10^5$ times smaller than τ_y, for all values of δ considered. In all of the following calculations, we use $\delta = 0.01$ μm to ensure good convergence.

B. General Trapping Properties in Two Parallel Beams

As in the previous section, the cylinder is trapped symmetrically in two beams of equal power, located such that their focal points lie 0.3 μm inside its ends, i.e., with a trap separation of 4.4 μm. Two polarization states are considered: The $\perp$ and $\parallel$ subscripts indicate polarization of the electric field perpendicular and parallel to the cylinder axis, respectively. The forces and torques, resulting from deviations from the equilibrium position in each of the five coordinates, are considered independently and shown in Fig. 3.

It can be seen that the forces act in accordance with the qualitative arguments outlined above. For example, positioning the rod so that it lies perpendicular to the beam axes, along the line connecting their foci, ensures that there are no excess torques, and that the horizontal components of the force, f_x and f_y, are zero, i.e., the relevant curves in Fig. 3 pass through the origin. When the cylinder is translated away from equilibrium, in the horizontal plane, perpendicular mirror planes are disrupted, and restoring forces are induced [see f_x in Fig. 3(a) and f_y in Fig. 3(b)]. The vertical force f_z, vanishes when the vertical position is such that the scattering force is compensated for
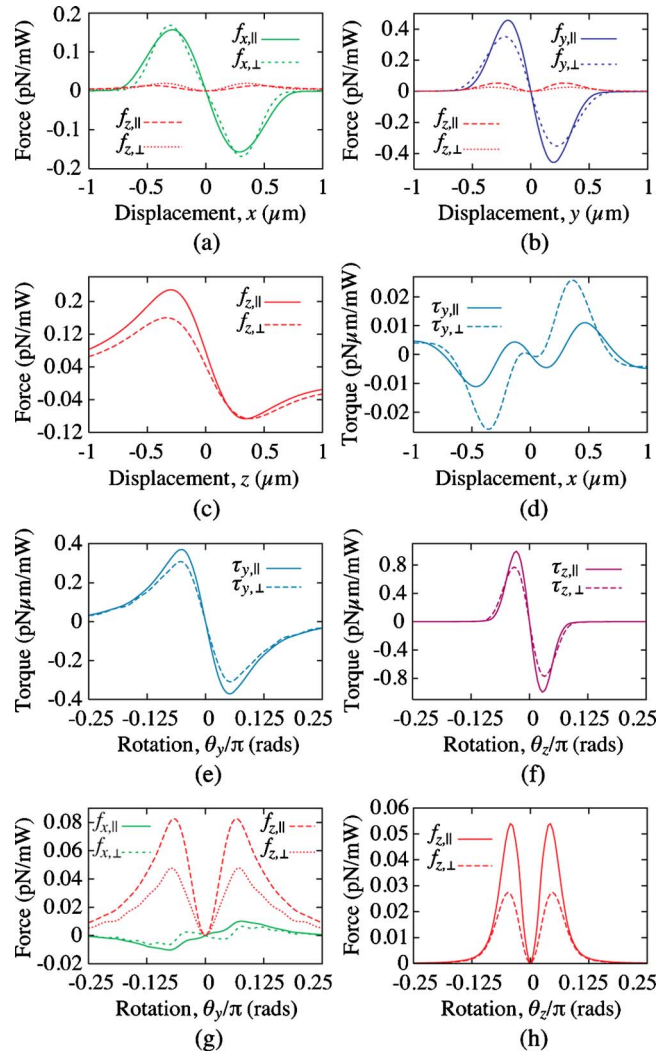

Fig. 3. (Color online) Calculations of induced forces and torques on the cylinder in two parallel Gaussian beams as functions of (a)–(d) translational and (e)–(h) rotational displacements from its initial position.

by the intensity gradients, i.e., at the trapping height [see Fig. 3(c)]. As expected, displacements from this point also produce a restoring force.

Torques can also be induced about axes that do not appear in the remaining mirror plane. For example, a displacement in the x-direction induces a torque about the y-axis [Fig. 3(d)]. An analogous effect is not observed for displacements in the y-direction since it is prohibited *a priori* by the rotational symmetry of the cylinder.

The effect of rotating the rod is directly analogous to the displacements. Rotations are met by restoring torques [Figs. 3(e) and 3(f)] and, in the case of rotations about the y-axis, a force in the x-direction is produced [Fig. 3(g)]. The translations parallel to x and y, and the rotations θ_y and θ_z, each disturbs the vertical equilibrium of the particle and give rises to vertical forces. These forces differ from restoring forces in that they are even functions of the displacement [see Figs. 3(a), 3(b), 3(g), and 3(h)].

The velocities with which these forces are associated can be found by dividing by the appropriate element of the hydrodynamic resistance. The maximum translation

velocity in the x-direction, for instance, is $\approx 11.5~\mu$m/mW s, while that in the y-direction is $\approx 22~\mu$m/mW s; although the friction is greater for a translation in the y-direction, the stiffness is proportionately even greater [compare Figs. 3(a) and 3(b)]. Figure 3(d) also reveals that, as the cylinder is dragged in the x-direction, i.e., along its length, it feels a torque about the y-axis. While this torque is initially small, it becomes sizable as the displacement of the cylinder causes it to lose contact with the trailing beam. This renders such a configuration unstable. For these reasons, it is almost always preferable to drag cylinders in the direction normal to their axes. On reaching its destination it can be rotated, as desired, about the z-axis at a maximum rate of ≈ 3.5 Hz/mW, according to the maximum torque acquired in Fig. 3(f).

The form of the stiffness matrix, **K** in Eq. (2), is constrained by the symmetry of the force density. The behavior of the induced forces has been discussed (Fig. 3). Provided that these forces are not even functions of the displacement, their first derivatives will be nonzero and will appear in **K**. For the beam arrangements considered here, the components of **K** are

$$\mathbf{K^{tt}} = \begin{pmatrix} K_{xx}^{tt} & 0 & 0 \\ 0 & K_{yy}^{tt} & 0 \\ 0 & 0 & K_{zz}^{tt} \end{pmatrix}, \quad \mathbf{K^{rr}} = \begin{pmatrix} 0 & 0 & 0 \\ 0 & K_{yy}^{rr} & 0 \\ 0 & 0 & K_{zz}^{rr} \end{pmatrix},$$

$$\mathbf{K^{tr}} = \begin{pmatrix} 0 & K_{xy}^{tr} & 0 \\ 0 & 0 & 0 \\ 0 & 0 & 0 \end{pmatrix}, \quad \mathbf{K^{rt}} = \begin{pmatrix} 0 & 0 & 0 \\ K_{yx}^{rt} & 0 & 0 \\ 0 & 0 & 0 \end{pmatrix}. \quad (11)$$

C. Beam Separation
It might be expected that the separation between the beams might influence the optically induced forces. Figure 4(a) shows the x-component of the force induced by displacements in the same direction for a range of beam separations. When the beams are close together, the induced force has a maximum magnitude that varies only weakly with the beam separation. The displacement for which these maxima occur, however, is greater, the lower is the separation between the beams, because a larger translation is needed before the beam reaches the end of the cylinder. As the beam separation increases, the maxima occur for successively smaller displacements and decrease in magnitude. Finally, for the largest separation, $5~\mu$m, equal to the length of the cylinder, they change in sign. As may be confirmed from Fig. 4(a), these variations combine to produce a stiffness that initially increases, as the trapping beams are separated, reaches a maximum value, and then decreases before changing sign, rendering the equilibrium unstable.

Displacements in the y-direction lead to a different behavior [Fig. 4(b)]. When the beams are close together the maximum reverse force and the stiffness are both at their largest and are relatively invariant with respect to the increasing separation. However, as the beams approach the tips of the cylinder both of these quantities decrease in value.
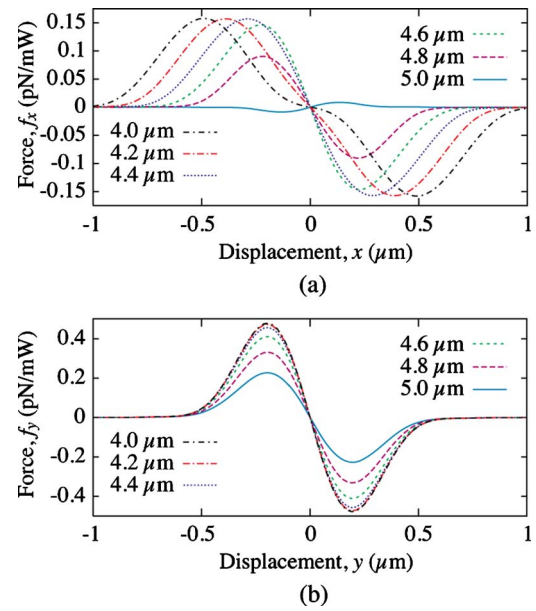

Fig. 4.   (Color online) Restoring forces acting on a cylinder in two traps for displacement in the (a) x- and (b) y-directions, for different separations between the beams. The beam polarization is parallel to the cylinder axis.

The effect of the beam separation on the trapping properties can be seen more clearly in Fig. 5, which shows the equilibrium trapping height z_{eqm} and elements of the stiffness matrix [Eq. (11)] as functions of the beam separation for a cylinder trapped in two parallel beams polarized parallel to the cylinder axis. When the beams are close, they interfere and the resulting effect on the trapping height can be seen in Fig. 5(a). However, the effect on the stiffness coefficients is scarcely noticeable. The translational stiffnesses perpendicular to the cylinder axis, K_{yy}^{tt} and K_{zz}^{tt} [Fig. 5(b)], remain constant as the beam separation increases until the beams start to "feel" the ends of the cylinder. At this point K_{yy}^{tt} and K_{zz}^{tt} start to diminish. Parallel to the cylinder axis, as was presaged in Fig. 4(a), the magnitude of the stiffness, K_{xx}^{tt}, increases rapidly, reaching a maximum at a separation of 4.6 μm before decreasing and changing sign. Since K_{xx}^{tt} cannot be maximized simultaneously with K_{yy}^{tt} and K_{zz}^{tt}, the most appropriate choice of the beam configuration depends on the manipulations to be performed.

The rotational stiffnesses, K_{yy}^{rr} and K_{zz}^{rr}, behave in a similar manner to the translational ones [Fig. 5(c)]. As the distance between the beams increases, so does the torque that they apply in response to small rotations. This continues until the beams encounter the ends of the cylinder and their efficacy reduces. Figure 5(d) shows a detail from Fig. 5(c). When the beams are almost coincident, the induced torque acts as it would for a single beam. As in the case of prolate spheroids [19], cylinders experience two competing demands: The first is to align with the elongated intensity profile along the beam axis, and the second is to align with the polarization direction. These effects are captured in Fig. 5(d). When the beams are superimposed, the horizontal configuration is unstable and K_{yy}^{rr} is positive. However, K_{zz}^{rr} remains negative owing to the polarization-induced torque.
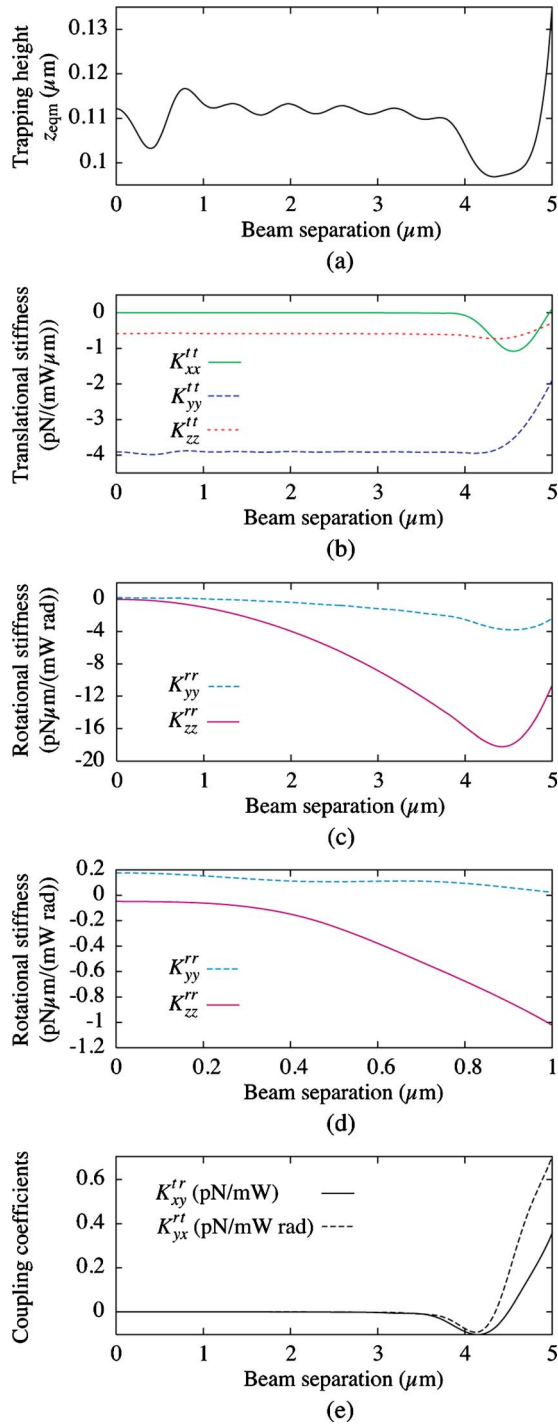
Fig. 5.   (Color online) Calculations of (a) the equilibrium trapping height and (b)–(e) the stiffness coefficients of a 5 μm long 0.2 μm radius cylinder trapped in two parallel beams as functions of the beam separation.

Figure 5(e) shows the cross terms in the stiffness matrix, K_{xy}^{tr} and K_{yx}^{rt}. They are of similar magnitudes, diverging as the beam separation increases. Both are relatively small, and less meaningful, quantities than the other stiffness coefficients. In the case of the simple restoring forces, the linear approximation retains its validity for translations up to ∼0.2 μm or rotations up to ∼0.05π rad (see Fig. 3), i.e., a significantly wider range than that expected of its thermally induced motion [4]. In contrast, for

the cross terms the linear approximation retains its validity over a noticeably smaller range of displacements [see Figs. 3(d) and 3(g)].

D. Multiple Beams
With holographic optical trapping, an almost infinite range of beam configurations is available to the user. We consider two further examples. In Fig. 6 the cylinder is, once more, trapped symmetrically in a linear arrangement of parallel beams. This time the number of trapping beams is varied between two and five. The outermost beams are placed 0.3 μm from the ends of the cylinder and the other beams are spaced equally in between. The figure shows the restoring torque τ_z per milliwatt of the total incident optical power, as the cylinder is rotated about the z-axis. Evidently, the major effect is in accordance with intuition. The angular range over which the beams apply a significant restoring torque increases with the number of beams because the angular range spanned by beams closer to the center of the cylinder is commensurately greater. Simultaneously K_{zz}^{rr} decreases as does the maximum restoring torque, because the optical power is distributed more widely. Increasing the number of beams has a similar effect on τ_y (not shown).

The other noteworthy change is that the restoring force parallel to the cylinder axis is systematically degraded on increasing the number of beams, since the outer beams alone dictate the restoring forces in this direction, and they possess proportionally less power. Qualitatively similar effects were reported from FDTD calculations [14] confirming that the two beams closest to the ends of the cylinder contribute most strongly to the formation of the trap. Therefore, for most applications a pair of traps close to the ends of the cylinder appears to be the most useful configuration.

Other beam positions can produce more complicated coupling effects. By breaking the symmetry of the incident beam configuration, a wider range of forces and torques are permitted, and the form of the stiffness matrix changes. The possibility of observing relatively complicated stochastic dynamics presents itself but, beyond this, such traps are of little obvious practical value. As an illustration we consider a cylinder held in three parallel beams. The two outermost beams are located at 0.3 μm from the ends of the cylinder, while the middle beam is
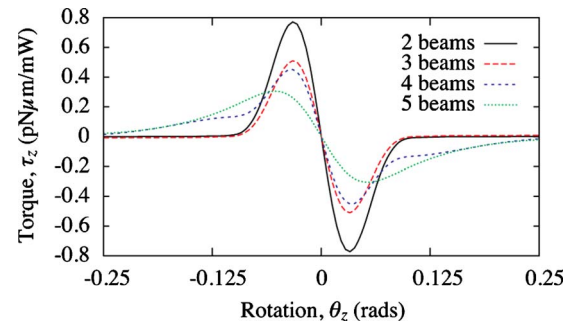

Fig. 6.   (Color online) The torque about the beam axis, τ_z, experienced by a cylinder with a length of 5 μm and a radius of 0.25 μm symmetrically trapped in a linear parallel array of beams. The beams are polarized perpendicular to the cylinder axis.

positioned at $x = +1.1$ μm from the center. Because of the asymmetric environment, the equilibrium trapping position is inclined slightly to the horizontal and displaced slightly parallel to the x-axis. The precise position is found to be $z_{eqm} = 0.1024$ μm, $x_{eqm} = 6.69 \times 10^{-4}$ μm, and $\theta_y = -9.8 \times 10^{-4}$ rad, with the remaining coordinates being identically zero for symmetry reasons. These deviations are extremely small, but have some minor effects on the induced forces if they are neglected.

Spoiling the symmetry in this simple way alters the forces and torques that are induced by simple coordinate displacements. In fact the additional coupling mechanisms precipitated by this change are numerous. In its equilibrium configuration the system contains a vertical mirror plane and when the displacement of the rod preserves this mirror plane, i.e., if the rod is translated vertically or rotated in the vertical plane, there is a restriction on the forces and torques that may be induced (i.e., $f_y = 0$, $\tau_x = \tau_z = 0$). Apart from this restriction, any particular displacement may give rise to all possible forces. The most significant example is the displacement in the y-direction, which leads to a restoring force and also to smaller forces in the x- and z-directions [see Fig. 7(a)]. Torques are also induced about the y- and z-axes [Fig. 7(b)].

5. DISCUSSION

In the preceding pages we have presented the results of DDA calculations of the optical forces and torques experienced by a dielectric cylinder trapped horizontally by two or more beams. It has been shown that, for most purposes, trapping is best achieved by two beams, focused just within the ends of the cylinder. Many of the results can be interpreted in the light of the electromagnetic force density given in Eq. (1a). These densities are concentrated on the surface of the cylinder, are proportional to the total intensity at the surface, and are directed parallel to the surface normal.

The forces and torques that can exist in any particular system are subject to the symmetry of the force density distribution. Forces perpendicular to a mirror plane must be zero as must the torque about any axis in the plane. Forces and torques perpendicular to a cylindrical symmetry axis must also vanish. When not subject to either of these restrictions forces will only vanish under special conditions, for example, when scattering forces are counterbalanced by forces introduced by intensity variations in the incident radiation.

As a result, a cylinder can be trapped horizontally in a symmetric linear arrangement of parallel beams so that the displacement (parallel to x, y, or z) or the rotation (θ_y or θ_z) is met by a restoring force or torque. In addition, vertical forces (parallel to the z-axis) are induced by all such movements, but with the exception of displacements in the z-direction these are even functions of the displacement and, consequently, do not generate a restoring force. Because it is not prohibited by symmetry, rotational-translational couplings also occur so that, for example, the displacement in the x-direction produces a torque about the y-axis, in addition to the restoring and vertical forces already discussed. Similarly, rotation about the y-axis also produces a force in the x-direction.

From the point of view of micromanipulation, these coupling effects mean that it is preferable to drag the cylinder in the transverse direction, rather than parallel to its length. This is because, in addition to the instability mentioned above, the maximum force that may be applied is over twice as big perpendicular to the cylinder axis compared with parallel to it. Although the friction coefficient is also greater perpendicular to the axis, it is only approximately 1.5 times the size so that, for this cylinder, the transverse motion is potentially faster than, as well as more stable than, the longitudinal motion.

Polarization has also been seen to influence the induced forces. For non-absorbing optically isotropic dielectrics the force density is always normal to a material boundary [see Eq. (1a)]. Since the electric field component parallel to a dielectric surface is continuous, while the perpendicular component is discontinuous, one would expect that, for a weakly scattering object, forces generated with the parallel polarization would tend to be greater. This idea is borne out in Fig. 3 where, for example, the restoring forces in the y- and z-directions have greater maxima when the field is polarized in the x-direction.

Taking the gradient of the induced force with respect to displacement gives components of the stiffness matrix **K**. Its form is subject to the same symmetry conditions as those described above. As a result, the stiffness matrix for a cylinder, in a symmetric arrangement of parallel beams with collinear focal points, has five diagonal entries; the sixth, relating to the rotation about its axis, is eliminated by the rotational symmetry of the object. Both of the translational-rotational coupling processes that are found are also odd with respect to their respective displacements and therefore appear in **K** as well.

These additional entries in **K** can affect the stability of the trap. In the absence of thermal forces, the equation of
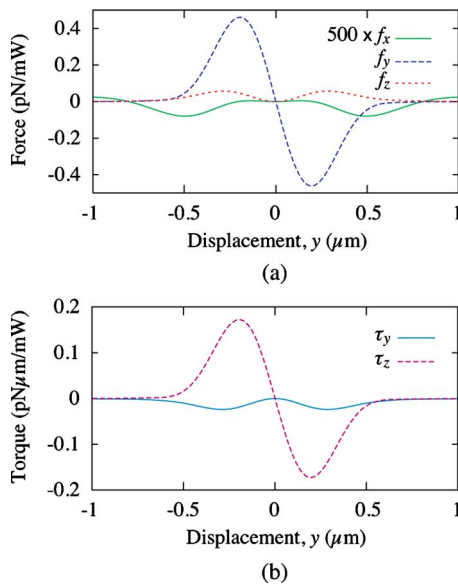

Fig. 7. (Color online) Induced (a) forces and (b) torques as functions of y-displacement, for a cylinder trapped in an asymmetric arrangement of three parallel beams with collinear foci. The displacement is measured relative to the trapping coordinates (see text).

motion of an arbitrary object, harmonically bound in an optical trap with respect to its position and orientation, is $\zeta \dot{q} = \mathbf{K}q$ in the vicinity of mechanical equilibrium [4] (ζ is the hydrodynamic friction matrix and q is a generalized displacement vector comprising three translational and three rotational coordinates). This system will be stable if and only if all of the eigenvalues of $\zeta^{-1}\mathbf{K}$ are less than zero [46]. However, coupling coefficients in $\mathbf{K}$ can cause this condition to be violated even when the diagonal entries, responsible for the simple restoring forces, are all negative. To have this effect, the coupling coefficients need to be larger than in the present case. Nevertheless, the idea that the stability of an optical trap could be jeopardized by the shape rather than the refractive index warrants further examination.

It is also noteworthy that $K_{xy}^{tr} \neq K_{yx}^{rt}$ so that $\mathbf{K}$ is not symmetric. If the system were conservative, the force field could be obtained from an underlying potential U. In this case, $\mathbf{K}$ would be the Hessian of U evaluated at equilibrium and would therefore be symmetric (i.e., $\partial^2 U/\partial x\,\partial y = \partial^2 U/\partial y\,\partial x$, etc.). Therefore the observed difference between K_{xy}^{tr} and K_{yx}^{rt} is an expression of the non-conservative nature of optically induced force fields.

That these force fields are not conservative has been understood for some time [47]. Non-conservative effects, as they relate to optically trapped spheres, have been analyzed more recently [48]. It has been shown that the probability distribution of an optically trapped sphere contains finite probability currents which persist for all time. Analogous effects will occur for non-spherical particles but the manifestation, in terms of the force field, is fundamentally different. The gradient of the force field of a sphere at mechanical equilibrium, i.e., its stiffness, is necessarily symmetric and, within the linear approximation, the curl of the force vanishes and the field appears approximately conservative. However, for non-spherical particles, even for small displacements, the non-conservative nature of the field is explicitly manifested in asymmetries in the derivative of the force. The effect is small for the cylinders studied here, but this need not generally be the case, and will form an interesting subject for future study.

6. CONCLUSION

The optical trapping properties of a silica microrod, held horizontally in two or more linearly polarized Gaussian beams, have been investigated using the discrete dipole approximation (DDA). Induced forces and torques have been evaluated as functions of the displacement. The generalized trap stiffness $\mathbf{K}$, an order 6 matrix given by the gradient of the forces and torques with respect to translational and rotational coordinates, has been evaluated under a variety of conditions. The observed behavior has been interpreted in terms of the optical force density and has been seen to be in accordance with related symmetry conditions. It has been found that the cylinder is most effectively trapped by two parallel beams with their focal regions falling just inside the ends of the cylinder. A subsequent calculation of the hydrodynamic resistance of the cylinder reveals that the most rapid and stable way of translating the cylinder is in the horizontal direction perpendicular to its axis. More fundamentally, it has been shown that the form of the stiffness matrix depends on the arrangement of beams and, in general, it is neither diagonal nor symmetric. This implies that the optical force field is non-conservative, which has interesting ramifications which will be explored further in a future publication.

APPENDIX A

The equation for the CSP Gaussian beam used in these simulations is

$$\mathbf{E} = \left(g(kR) + [f(kR) - g(kR)]\frac{x^2}{R^2} + \frac{i}{2}f(kR)kz' \right)\hat{x}$$
$$+ \left([f(kR) - g(kR)]\frac{xy}{R^2} \right)\hat{y} + \left([f(kR) - g(kR)]\frac{xz'}{R^2} \right.$$
$$\left. - \frac{i}{2}f(kR)kx \right)\hat{z}, \tag{A1}$$

where $z' = z - iz_0$ so that R is given by

$$R = (x^2 + y^2 + z'^2)^{1/2}. \tag{A2}$$

k is the modulus of the wavevector in the medium and the scalar functions f and g are

$$f(kR) = j_0(kR) + j_2(kR),$$

$$g(kR) = j_0(kR) - \frac{1}{2}j_2(kR), \tag{A3}$$

where j_n is a spherical Bessel function of the first kind, of order n. The real scalar quantity z_0 is the position of the complex source and determines, among other attributes, the beam waist [38].

ACKNOWLEDGMENTS

REFERENCES

1. S. H. Simpson and S. Hanna, "Rotation of absorbing spheres in Laguerre–Gaussian beams," J. Opt. Soc. Am. A **26**, 173–183 (2009).
2. S. H. Simpson and S. Hanna, "Optical angular momentum transfer by Laguerre–Gaussian beams," J. Opt. Soc. Am. A **26**, 625–638 (2009).
3. A. Rohrbach, "Stiffness of optical traps: quantitative agreement between experiment and electromagnetic theory," Phys. Rev. Lett. **95**, 168102 (2005).
4. S. H. Simpson and S. Hanna, "Thermal motion of a holographically trapped SPM-like probe," Nanotechnology **20**, 395710 (2009).
5. K. Berg-Sorensen and H. Flyvbjerg, "Power spectrum analysis for optical tweezers," Rev. Sci. Instrum. **75**, 594–612 (2004).
6. N. B. Viana, A. Mazolli, P. A. M. Neto, H. M. Nussenzveig, M. S. Rocha, and O. N. Mesquita, "Absolute calibration of optical tweezers," Appl. Phys. Lett. **88**, 131110 (2006).

7. E.-L. Florin, A. Pralle, E. H. K. Stelzer, and J. K. H. Hörber, "Photonic force microscope calibration by thermal noise analysis," Appl. Phys. A **66**, S75–S78 (1998).

8. Y. Nakayama, P. J. Pauzauskie, A. Radenovic, R. M. Onorato, R. J. Saykally, J. Liphardt, and P. Yang, "Tunable nanowire nonlinear optical probe," Nature **447**, 1098–1101 (2007).

9. H. Kress, E. H. K. Stelzer, and A. Rohrbach, "Tilt angle dependent three-dimensional-position detection of a trapped cylindrical particle in a focused laser beam," Appl. Phys. Lett. **84**, 4271–4273 (2004).

10. T. Yu, F. Cheong, and C. Sow, "The manipulation and assembly of CuO nanorods with line optical tweezers," Nanotechnology **15**, 1732–1736 (2004).

11. L. Ikin, D. M. Carberry, G. M. Gibson, M. J. Padgett, and M. J. Miles, "Assembly and force measurement with SPM-like probes in holographic optical tweezers," New J. Phys. **11**, 023012 (2009).

12. R. Agarwal, K. Ladavac, Y. Roichman, G. H. Yu, C. M. Lieber, and D. G. Grier, "Manipulation and assembly of nanowires with holographic optical traps," Opt. Express **13**, 8906–8912 (2005).

13. T. L. Min, P. J. Mears, L. M. Chubiz, I. Golding, Y. R. Chemla, and C. V. Rao, "High-resolution, long-term characterization of bacterial motility using optical tweezers," Nat. Methods **6**, 831–835 (2009).

14. D. Benito, S. H. Simpson, and S. Hanna, "FDTD simulations of forces on particles during holographic assembly," Opt. Express **16**, 2942–2957 (2008).

15. J.-Q. Qin, X.-L. Wang, D. Jia, J. Chen, Y.-X. Fan, J. Ding, and H.-T. Wang, "FDTD approach to optical forces of tightly focused vector beams on metal particles," Opt. Express **17**, 8407–8416 (2009).

16. D. A. White, "Numerical modeling of optical gradient traps using the vector finite element method," J. Comput. Phys. **159**, 13–37 (2000).

17. T. A. Nieminen, V. L. Y. Loke, A. B. Stilgoe, G. Knoener, A. M. Branczyk, N. R. Heckenberg, and H. Rubinsztein-Dunlop, "Optical tweezers computational toolbox," J. Opt. A, Pure Appl. Opt. **9**, S196–S203 (2007).

18. S. H. Simpson and S. Hanna, "Numerical calculation of inter-particle forces arising in association with holographic assembly," J. Opt. Soc. Am. A **23**, 1419–1431 (2006).

19. S. H. Simpson and S. Hanna, "Optical trapping of spheroidal particles in Gaussian beams," J. Opt. Soc. Am. A **24**, 430–443 (2007).

20. A. B. Stilgoe, T. A. Nieminen, G. Knoner, N. R. Heckenberg, and H. Rubinsztein-Dunlop, "The effect of Mie resonances on trapping in optical tweezers," Opt. Express **16**, 15039–15051 (2008).

21. L. Novotny, R. X. Bian, and X. S. Xie, "Theory of nanometric optical tweezers," Phys. Rev. Lett. **79**, 645–648 (1997).

22. P. W. Barber, "Resonance electromagnetic absorption by nonspherical dielectric objects," IEEE Trans. Microwave Theory Tech. **25**, 373–381 (1977).

23. V. K. Varadan and V. V. Varadan, eds., *Acoustic, Electromagnetic and Elastic Wave Scattering: Focus on the T-matrix Approach* (Pergamon, 1980).

24. B. T. Draine and P. J. Flatau, "Discrete-dipole approximation for scattering calculations," J. Opt. Soc. Am. A **11**, 1491–1499 (1994).

25. M. A. Yurkin and A. G. Hoekstra, "The discrete dipole approximation: an overview and recent developments," J. Quant. Spectrosc. Radiat. Transf. **106**, 558–589 (2007).

26. P. C. Chaumet, A. Rahmani, and M. Nieto-Vesperinas, "Optical trapping and manipulation of nano-objects with an apertureless probe," Phys. Rev. Lett. **88**, 123601 (2002).

27. D. Bonessi, K. Bonin, and T. Walker, "Optical forces on particles of arbitrary shape and size," J. Opt. A, Pure Appl. Opt. **9**, S228–S234 (2007).

28. J. Trojek, V. Karasek, and P. Zemanek, "Extreme axial optical force in a standing wave achieved by optimized object shape," Opt. Express **17**, 10472–10488 (2009).

29. A. Penttila, E. Zubko, K. Lumme, K. Muinonen, M. A. Yurkin, B. Draine, J. Rahola, A. G. Hoekstra, and Y. Shkuratov, "Comparison between discrete dipole implementations and exact techniques," J. Quant. Spectrosc. Radiat. Transf. **106**, 417–436 (2007).

30. B. T. Draine, "The discrete-dipole approximation and its application to interstellar graphite grains," Astrophys. J. **333**, 848–872 (1988).

31. P. C. Chaumet and M. Nieto-Vesperinas, "Time-averaged total force on a dipolar sphere in an electromagnetic field," Opt. Lett. **25**, 1065–1067 (2000).

32. A. Greenbaum, *Iterative Methods for Solving Linear Systems* (SIAM, 1997).

33. R. W. Freund, "Conjugate gradient-type methods for linear-systems with complex symmetrical coefficient matrices," SIAM (Soc. Ind. Appl. Math.) J. Sci. Stat. Comput. **13**, 425–448 (1992).

34. P. C. Chaumet, A. Rahmani, A. Sentenac, and G. W. Bryant, "Efficient computation of optical forces with the coupled dipole method," Phys. Rev. E **72**, 046708 (2005).

35. P. C. Chaumet and C. Billaudeau, "Coupled dipole method to compute optical torque: application to a micropropeller," J. Appl. Phys. **101**, 023106 (2007).

36. J. J. Goodman, B. T. Draine, and P. J. Flatau, "Application of fast Fourier transform techniques to the discrete-dipole approximation," Opt. Lett. **16**, 1198–1200 (1991).

37. M. Frigo and S. G. Johnson, "The design and implementation of FFTW3," Proc. IEEE **93**, 216–231 (2005).

38. C. J. R. Sheppard and S. Saghafi, "Electromagnetic Gaussian beams beyond the paraxial approximation," J. Opt. Soc. Am. A **16**, 1381–1386 (1999).

39. A. L. Cullen and P. K. Yu, "Complex source-point theory of the electromagnetic open resonator," Proc. R. Soc. London, Ser. A **366**, 155–171 (1979).

40. W. H. Press, S. A. Teukolsky, W. T. Vetterling, and B. P. Flannery, *Numerical Recipes: The Art of Scientific Programming*, 3rd ed. (Cambridge U. Press, 2007).

41. M. Abramowitz and I. A. Stegun, eds., *Handbook of Mathematical Functions with Formulas, Graphs and Mathematical Tables* (Dover, 1965).

42. J. M. García Bernal and J. García de la Torre, "Transport-properties and hydrodynamic centers of rigid macromolecules with arbitrary shapes," Biopolymers **19**, 751–766 (1980).

43. B. Carrasco and J. García de la Torre, "Hydrodynamic properties of rigid particles: comparison of different modeling and computational procedures," Biophys. J. **76**, 3044–3057 (1999).

44. L. S. Blackford, J. Choi, A. Cleary, E. D'Azevedo, J. Demmel, I. Dhillon, J. Dongarra, S. Hammarling, G. Henry, A. Petitet, K. Stanley, D. Walker, and R. C. Whaley, *ScaLAPACK Users Guide* (SIAM, 1997).

45. J. Happel and H. Brenner, *Low Reynolds Number Hydrodynamics: With Special Applications to Particulate Media*, 2nd ed. (Noordhoff International, 1973).

46. D. W. Jordan and P. Smith, *Nonlinear Ordinary Differential Equations: An Introduction to Dynamical Systems*, 3rd ed. (Oxford U. Press, 1999).

47. A. Ashkin, J. M. Dziedzic, J. E. Bjorkholm, and S. Chu, "Observation of a single-beam gradient force optical trap for dielectric particles," Opt. Lett. **11**, 288–290 (1986).

48. Y. Roichman, B. Sun, A. Stolarski, and D. G. Grier, "Influence of nonconservative optical forces on the dynamics of optically trapped colloidal spheres: The fountain of probability," Phys. Rev. Lett. **101**, 128301 (2008).